Effect of Preparation Mode on the Properties of Mn-Na-W/SiO$_2$ Catalysts for Oxidative Coupling of Methane: Conventional Methods vs. POSS Nanotechnology

I.Z. Ismagilov[1], E.V. Matus[1], V.V. Kuznetsov[1], M.A. Kerzhentsev[1], S.A. Yashnik[1], T.V. Larina[1], I.P. Prosvirin[1], R.M. Navarro[2], J.L.G. Fierro[2], G. Gerritsen[3], H.C.L. Abbenhuis[3], Z.R. Ismagilov[1,4]*

[1]Boreskov Institute of Catalysis SB RAS, pr. Akademika Lavrentieva, 5, 630090, Novosibirsk, Russia
[2]Instituto de Catálisis y Petroleoquímica, CSIC, Marie Curie 2, 28049, Madrid, Spain
[3]Hybrid Catalysis B.V., Den Dolech 2, Eindhoven 5612, AZ, the Netherlands
[4]Institute of Coal Chemistry and Material Science SB RAS, pr. Sovetskiy, 18, 650000, Kemerovo, Russia

Abstract

Using XPS, BET, XRD, TG-DTA, HRTEM-EDX, TPR and UV-Vis Diffuse Reflectance spectroscopic methods the electronic, redox and structural properties of Mn-Na-W/SiO$_2$ catalysts prepared by the incipient wetness impregnation method and mixture slurry method were studied in detail. Since POSS nanotechnology (POSS = polyhedral oligomeric silsesquioxanes) has attracted attention as tooling for synthesis of catalysts with novel properties and functionalities, we expanded this method for the preparation of Mn-Na-W/SiO$_2$ catalyst. The physicochemical and catalytic properties of Mn-Na-W/SiO$_2$ catalysts prepared by conventional methods and POSS nanotechnology were examined comparatively. In all studied Mn-Na-W/SiO$_2$ catalysts both individual oxides (MnO$_x$, WO$_3$) and bimetal oxide phases (Na$_2$WO$_4$, MnWO$_4$) are found in addition to oxide particles of high dispersion. The UV-Vis Diffuse Reflectance indicates that Na$^+$ cations facilitates stabilization of octahedrally coordinated Mn$^{3+}_{Oh}$ cations in the isolated state, while Mn$^{3+}_{Oh}$ promote the disordering of W^{6+} cations in the supported system. The Mn-Na-W/SiO$_2$ prepared using metal-POSS precursors marks out presence of unglobular SiO$_2$ particles, higher dispersion of MnO$_x$ and MnWO$_4$ particles and more easily reducible metal-oxide species. The catalysts prepared by incipient impregnation method and mixture slurry method have practically similar catalytic performance while the catalyst prepared by POSS nanotechnology method shows lower activity and selectivity. At 800–850 °C the increase of C$_2$ hydrocarbons yield from 4 to 15% and the rise of molar ratio C$_2$H$_4$/C$_2$H$_6$ from 0.2 to 1 are observed when impregnation or mixture slurry method are used for catalyst preparation instead of POSS nanotechnology method.

1. Introduction

Development of effective catalysts for conversion of methane to valuable products with high selectivity will solve such problems as rational utilization of natural gas and environmental protection [1–10]. The oxidative coupling of methane (OCM) is a promising process for direct production of ethane and ethylene [8–10]. Besides the selective reactions (Eqs. (1) and (2)), there are nonselective oxidation of the hydrocarbons to CO$_x$ by-products (Eq. 3).

$$2CH_4 + 0.5O_2 \rightarrow C_2H_6 + H_2O \qquad (1)$$

$$2CH_4 + O_2 \rightarrow C_2H_4 + 2H_2O \qquad (2)$$

$$CH_4 + 2O_2 \rightarrow CO_2 + 2H_2O \qquad (3)$$

The OCM process is a combination of the heterogeneous catalytic and homogeneous noncatalytic reactions [11, 12]. On the whole, the role of catalytic surface is the generation of methyl radicals, as well as the suppression of nonselective surface oxidation of hydrocarbons to carbon oxides. A large number of catalytic systems have been studied and ~25% C$_2$ (C$_2$H$_6$ + C$_2$H$_4$) yields have been obtained

---

that is close to the commercial usefulness [10, 13, 14]. The Mn-Na-W/SiO$_2$ catalyst is one of the suitable OCM catalysts that shows both high product yield and long-term stability [10, 13, 14].

The complex reaction mechanism of OCM and multicomponent composition of Mn-Na-W/SiO$_2$ catalyst complicate the elucidation of the role of various components of this catalyst. So there are some controversies concerning the structure of active center in the Mn-Na-W/SiO$_2$ catalytic system. The surface cluster species WO$_4$ with one W=O and three W-O-Si bonds was one of the first model of the active site suggested for this reaction [15]. The DFT-study of Mn-Na-W/SiO$_2$ confirmed the possibility of tetrahedral WO$_4$ species to be active sites for methane activation [16]. By comparison of the catalytic behaviors of Mn/Na$_2$WO$_4$/MgO and NaMnO$_4$/MgO catalysts, the authors suggested that Na–O–Mn species were the most possible active sites [17]. The Mn$_2$O$_3$ species were proposed to act as the active sites responsible for the methane activation, while the Na$^+$ and oxo anion (WO$_4^{2-}$, MoO$_4^{2-}$, SO$_4^{2-}$, PO$_4^{3-}$ or P$_2$O$_7^{4-}$) affect the formation of the specified Mn species [18]. Alternatively, the two metal site model of active centers was considered by Li and co-workers on the basis of XANES, EXAFS, TPR, TPO and high temperature quenching EPR characterizations [19]. According to this model, methane activation takes place on the W^{6+} sites, while activation of gas-phase oxygen occurs on the Mn^{3+} sites. The oxygen spillover from Mn$_2$O$_3$ to Na$_2$WO$_4$ surface provides the higher activity of Mn-Na-W/SiO$_2$ catalyst in comparison with that of Na-W/SiO$_2$ one. The similar results were obtained by Kou et al. using the L-edge and the K-edge XAFS and XPS [20]. It was indicated that the combination of tetrahedral (WO$_4$) and octahedral (MnO$_6$) metallic cores with different oxidation states from each other is responsible for the catalysis in the oxidative coupling of methane. Ji et al. identified also that both Na-O-Mn and Na-O-W species act as the active centers of the catalysts for OCM [21]. It was noted that tetrahedral WO$_4$ species is more active and selective for the OCM reaction while the near-surface Mn concentration is correlated with the CH$_4$ conversion and C$_2$H$_4$ selectivity. There are different assumptions about the role of the alkali component [21–24]. In particular, it was demonstrated that Na induces the low temperature phase transition of amorphous silica support to α-cristobalite and also acts to disperse and stabilize the W surface species [22]. The Na presence was assumed to be necessary for the formation of distorted WO$_4$ species which are responsible for the catalyst activity [23]. In addition it was found that the presence of Na in the catalyst favors the Mn and W migration to the catalyst surface [21]. Thus, the structure of active centre for the OCM reaction is still a matter of discussion. However it is clear that the presence of all Mn, Na and W metals together provides the highest performance of Mn-Na-W/SiO$_2$ catalysts in the OCM reaction [21, 24]. The observed synergistic effect agrees with the two metal site model of active centers for the OCM reaction.

Various methods of preparation were applied for synthesis of the Mn-Na-W/SiO$_2$ catalyst: i) the incipient wetness impregnation method [22, 25, 26], ii) the mixture slurry method [25, 26], iii) the sol-gel method [25, 26], iv) the solid-phase synthesis [24] and v) the solution combustion method [27]. As the precursors of the active component, as a rule, inorganic salts of metals were used. It is obvious that variation of the metal content, the nature of the SiO$_2$ substrate or method and conditions of preparation allows regulation of the surface composition of catalyst, behavior of metal-metal and metal-support interaction, metal dispersion and distribution in support matrix and, consequently, the activity and stability of Mn-Na-W/SiO$_2$ catalyst [25, 28] in the target reaction. In particular, it was shown that the incipient wetness impregnation method provided the high concentration of Mn, Na and W elements on the catalyst surface, while the mixture slurry method and sol-gel method provided relatively uniform metal distribution between the surface and bulk of Mn-Na-W/SiO$_2$ catalyst [25]. It is suggested that uniform elemental concentrations counteracted the loss of active components during the reaction providing long-term stability of catalyst. The preparation method did not affect the phase composition of the catalyst, and Mn-Na-W/SiO$_2$ catalysts contain crystalline phases Mn$_2$O$_3$ of 60–80 nm in size, Na$_2$WO$_4$ of 50 nm in size and α-cristobalite [25, 27]. On the contrary, the metal content was shown to determine the phase composition of catalyst and the optimal metal content is equal to 0.5-3 wt.% Mn, 0.4–2.3 wt.% Na, 2.2–8.9 wt.% W [21].

The exploitation of the so-called "POSS nanotechnology" (POSS = polyhedral oligomeric silsesquioxanes) in which metal-containing silsesquioxanes are used as precursors for the preparation of catalytic materials provides a peculiar way to obtain nanosized catalysts [29, 30]. This method of preparing heterogeneous metal-containing materials has distinct advantage over traditional methods of preparing metal impregnated siliceous materials in that the metal atoms remain highly dispersed throughout support [29–35]. Maxim et al. reported that Mg, Al, Fe-Cr and Fe-containing microporous silicas were prepared by controlled calcination of

metallasilsesquioxanes in the presence of metal free silsesquioxane [32]. The isolated, clustered metal species as well as particles of iron oxide were revealed by spectroscopic analysis and TEM after thermolysis of Fe-silsesquioxanes in $20\%O_2/Ar$ at 500 °C. The study of the Cr- [33], Mg- [34] and Al-containing [34] silicas derived through calcination of appropriate metallsilsesquioxanes at similar conditions showed that nearly homogenous metal dispersion could be achieved. Only in case of Cr silicas the small amount of Cr_2O_3 was observed [33]. Obviously the increase of temperature of catalyst precursor calcination from 500 °C that is usually applied for calcination of metal-containing silsesquioxanes up to range 800–900 °C that is optimal for calcination of Na-Mn-W/SiO$_2$ material will lead to expected low dispersion of metal species. For example, the Ti-O-Si linkage remained when the titanosiloxane was subjected to calcination in the range 450–800 °C while the formation of anatase and rutile forms of TiO_2 was observed after calcination at temperature above 900 °C [35].

Herein using XPS, BET, XRD, TG-DTA, HR-TEM-EDX, TPR and UV-Vis Diffuse Reflectance spectroscopic methods we thoroughly studied electronic, redox and structural properties of Mn-Na-W/SiO$_2$ catalysts prepared by the incipient wetness impregnation method and the mixture slurry method. Since POSS nanotechnology has attracted attention as tooling for synthesis of catalysts with novel properties and functionalities [29–35] we expanded this method for the preparation of Mn-Na-W/SiO$_2$ catalyst. The physicochemical properties and performance in OCM of Mn-Na-W/SiO$_2$ catalysts prepared by conventional methods and POSS nanotechnology were examined comparatively. The peculiarity of the genesis of Mn-Na-W/SiO$_2$ materials prepared by different methods was revealed.

2. Experimental

2.1. Catalyst preparation

The series of Mn-Na-W/SiO$_2$ catalysts were synthesized at different preparation routes. The abbreviation in the bracket indicates the preparation method: I is the incipient wetness impregnation method, M is the mixture slurry method, and P is the POSS nanotechnology. The nominal metal components in the samples prepared by different methods were similar: 3 wt.% Mn, 1.4 wt.% Na and 5 wt.% W, which is in the range of optimal metals contents for the Mn-Na-W/SiO$_2$ tri-metallic catalyst [21].

The Mn-Na-W/SiO$_2$ (I) sample was prepared by sequential incipient wetness impregnation of SiO$_2$ (Silica gel Davisil 646, 250–500 μm, Sigma-Aldrich) with an aqueous solutions of the corresponding metal precursors (manganese (II) acetate tetrahydrate $Mn(CH_3COO)_2 \cdot 4H_2O$, sodium tungstate dihydrate $Na_2WO_4 \cdot H_2O$, sodium oxalate $Na_2C_2O_4$) taken in appropriate concentrations. The temperature of intermediate drying of Na-W/SiO$_2$ material (before following impregnation with solution of Mn salts) was 120 °C for 6 h. The Mn-Na-W/SiO$_2$ catalysts were then dried at 120 °C for 6 h and calcined in air at 850 °C for 6 h.

The Mn-Na-W/SiO$_2$ (M) catalyst was prepared by mixture slurry method. Aqueous solutions of salts (manganese (II) acetate tetrahydrate $Mn(CH_3COO)_2 \cdot 4H_2O$, sodium tungstate dihydrate $Na_2WO_4 \cdot 2H_2O$, sodium oxalate $Na_2C_2O_4$) taken in appropriate concentrations were added dropwise into a silica sol (LUDOX LS, 30 wt.% SiO$_2$, Sigma-Aldrich) with stirring, and the mixture was stirred vigorously for several hours. The mixture slurry was dried at 120 °C for 6 h and calcined in air at 850 °C for 6 h.

The Mn-Na-W/SiO$_2$ (P) sample was prepared by using metal-POSS precursors (manganese (II) heptaisobutylPOSS $(C_4H_9)_7Si_7O_9(OH)O_2Mn$, tungsten (IV) bis-heptaisobutylPOSS $((C_4H_9)_7Si_7O_{12})_2W$ and sodium heptaisobutylPOSS $(C_4H_9)_7Si_7O_9(OH)_2O-Na$). Metal-POSS precursors taken in the required ratio were dissolved in solvent (hexane-toluene mixture). Solvent removal was performed with a warm solution under Ar flow and using vigorous stirring. The catalysts were then dried at 120 °C for 6 h and calcined in air at 850 °C for 6 h.

The reference samples Mn/SiO$_2$, W/SiO$_2$, NaW/SiO$_2$, NaMn/SiO$_2$ and MnW/SiO$_2$ were prepared by sequential incipient wetness impregnation of SiO$_2$ (Silica gel Davisil 646, 250–500 μm, Sigma-Aldrich) with aqueous solutions of the corresponding metal precursors. The drying and calcination of the reference samples were performed in the same way as for sample obtained by impregnation method described above.

2.2. Catalyst characterization

The chemical composition of the prepared catalysts was determined by X-ray fluorescence spectroscopy (XFS) using an ARL analyzer with a Rh anode of an X-ray tube and inductively coupled plasma-atomic emission spectrometry (ICP-AES) method.

X-ray photoelectron spectra were recorded in a SPECS (Germany) spectrometer using a hemispherical PHOIBOS-150-MCD-9 analyzer (AlK$_\alpha$ radiation, hν = 1486.6 eV). The binding energy

(BE) scale was pre-calibrated using the positions of the peaks of Au4f$_{7/2}$ (BE = 84.0 eV) and Cu2p$_{3/2}$ (BE = 932.67 eV) core levels. The samples in the form of small granules were loaded onto a conducting double-sided copper scotch. The Si2p peak of SiO$_2$ catalyst support at 103.3 eV was used to correct charge effects on the sample. Survey spectra were recorded at the analyzer pass energy of 50 eV, and high resolution narrow energy windows at 20 eV. The atomic concentration ratios of elements on the catalyst surface were calculated from the integral photoelectron peak intensities (Mn2p, W4f, Na1s, O1s, C1s, Si2s), which were corrected with theoretical sensitivity factors based on the Scofield's photo-ionization cross sections [36].

The BET surface area (S$_{BET}$) and the pore volume (V$_{pore}$) of the supports and catalysts were determined in a Micromeritics ASAP 2400 instrument using nitrogen adsorption at -196 °C. Prior to surface area determination, the powders were degassed under vacuum (10^{-5} mbar) at 150 °C for 4 h.

The phase composition was determined by X-ray diffraction (XRD) in the 2-theta range of 10–80º using HZG-4C (Freiberger Prazisionmechanik) with a CoK$_\alpha$ radiation source.

The thermogravimetric and differential thermal analysis was carried out in a NETZSCH STA 449C apparatus. Catalysts were tested over the temperature range from room temperature up to 1000 °C at the heating rate of 10 °C/min in air.

Transmission electron microscopy (TEM) was carried out in a high-resolution JEOL JEM-2010 microscope operating at 200 kV with a structural resolution of 0.14 nm. The samples were deposited on perforated carbon supports attached to the copper grids. The local elemental analysis of the samples was carried out by an energy dispersive X-ray analysis (EDX) method using an EDAX spectrometer equipped with a Si (Li) detector with a resolution of 130 eV.

Temperature-programmed reduction (TPR) experiments were carried out in flow system with a quartz reactor (i.d. 4 mm). A 10 vol.% H$_2$/Ar mixture was used as a reduction gas. Prior to TPR, 100 mg catalyst sample was treated in O$_2$ at 500 °C for 0.5 h and then cooled down to room temperature. The reactor was heated at a rate of 10 °C/min to 950 °C. The effluent was analyzed by thermal conductivity detector (TCD).

The electronic state of Mn-Na-W/SiO$_2$ samples was studied by means of Ultraviolet-Visible-Near Infrared Diffuse Reflectance Spectroscopy (UV-Vis-NIR DRS) using a Shimadzu UV-2501 PC spectrophotometer with ISR-240A diffuse reflectance unit. All the samples were powdered and placed in a quartz cell with the optical path length of 2 mm. The diffuse reflectance spectra of the samples were recorded using BaSO$_4$ as the reflectance standard in the wavelength range of 190–900 nm at room temperature. The obtained coefficients of diffuse reflectance were transformed into absorption coefficients using the Kubelka-Munk function, $F(R_\infty) = (1-R_\infty)^2/2R_\infty$, and the wavelengths were converted into wave numbers. All UV-Vis-NIR DRS data are presented in the coordinates of Kubelka-Munk function vs wave numbers. UV-Vis-NIR DRS gives the way to reveal the oxidation degree of the cation, its coordination number, and the character of cations interaction with each other and with the support, using the *d-d* transitions in the visual part of the spectrum and the ligand-metal charge transfer bands (CTB) in the UV area.

2.3. Catalytic activity test

OCM experiments were performed in a 14 mm i.d. quartz fixed-bed reactor with a feed composition of CH$_4$: O$_2$: He equal to 4 : 1 : 2 under atmospheric pressure, at temperatures 650–950 °C and gas flow rate 175 mL$_N$/min. The gas purity was 99.95% CH$_4$, 99.995% O$_2$ and 99.995% He. Prior to each activity test, the catalysts were calcined in O$_2$ flow (100 mL$_N$/min) at 700 °C for 2 h. In order to minimize the catalyst overheating, the 500 mg sample (fraction of 0.25–0.50 mm) was diluted with an equal amount of SiC. Analysis of both inlet and outlet reaction mixtures were accomplished using the Stanford Research Systems QMS 300 mass spectrometric gas analyzer. Calculation of the reaction parameters was performed from mass flows considering the changing of the reaction volume, which can be determined from the change of inert concentration. Selectivity of the reaction products (C$_2$H$_6$, C$_2$H$_4$, CO and CO$_2$) was determined using flow rates (*V*) of products after the reactor as:

$$S_{C2H6} = \frac{2 \cdot V_{C2H6}}{2 \cdot V_{C2H6} + 2 \cdot V_{C2H4} + V_{CO} + V_{CO2}} \cdot 100\%$$

$$S_{C2H4} = \frac{2 \cdot V_{C2H4}}{2 \cdot V_{C2H6} + 2 \cdot V_{C2H4} + V_{CO} + V_{CO2}} \cdot 100\%$$

$$S_{CO} = \frac{V_{CO}}{2 \cdot V_{C2H6} + 2 \cdot V_{C2H4} + V_{CO} + V_{CO2}} \cdot 100\%$$

$$S_{CO2} = \frac{V_{CO2}}{2 \cdot V_{C2H6} + 2 \cdot V_{C2H4} + V_{CO} + V_{CO2}} \cdot 100\%$$

Yield of products was calculated as selectivity multiplied by methane conversion.

3. Result and discussion

3.1. Characterization of Mn-Na-W/SiO₂ catalysts

The actual metal bulk contents in the prepared Mn-Na-W/SiO₂ catalysts are shown in Table 1. It can be noted that in all cases the actual chemical composition of samples is in good agreement with nominal specified value – 3 wt.% Mn, 1.4 wt.% Na and 5 wt.% W.

The metal dispersion in Mn-Na-W/SiO₂ catalyst was estimated from XPS data. The surface atomic ratios obtained by XPS analysis are presented in Table 2. The surface Mn : Si ratios are similar to the bulk ratios for all samples indicating a high dispersion of Mn oxide in these catalysts. The surface Na : Si and W : Si ratios of all catalysts point out a less uniform distribution of these elements. The surface Na : Si and W : Si ratio is higher than the bulk ratio denoting that the Na and W are located preferentially on the silica surface rather than in the bulk. This effect is more pronounced for Mn-Na-W/SiO₂ (I) catalyst.

High resolution Mn2p, Na1s and W4f spectra of the fresh catalysts are shown in Fig. 1 and the binding energies (BE) of catalyst components are summarized in Table 3. Comparison of spectra in Fig. 1a indicates that the chemical states of Mn are similar in all studied samples. The Mn2p binding energy of 641.5 ± 0.1 is characteristic of the Mn^{3+} oxidation state on the surface [37, 38]. Na1s peak at 1071.8 ± 0.1 eV observed by XPS (Fig. 1b) indicates the Na^{+1} state [39]. The analysis of W4f spectra shows BE = 35.6 ± 0.1 eV expected for W^{6+} [40, 41], and the spectra of different catalysts are similar to each other (Fig. 1c). It is not possible to distinguish WO_3 and Na_2WO_4 phases by XPS because of identical W^{6+} state in both phases [36]. Thus, the data of XPS demonstrates that electronic states of Mn-Na-W/SiO₂ catalyst components on the surface are not affected by the catalyst preparation mode.

Table 1
The chemical composition and textural characteristics of Mn-Na-W/SiO₂ catalysts

Sample	Chemical composition, wt.%			Textural characteristics	
	Mn	Na	W	S_{BET}, (m²/g)	V_{pore}, (cm³/g)
Mn-Na-W/SiO₂ (I)	3.37	1.46	5.19	1.6	0.003
Mn-Na-W/SiO₂ (M)	3.01	1.55	4.83	0.9	0.002
Mn-Na-W/SiO₂ (P)	3.14	1.38	5.00	3.6	0.009

Table 2
Surface (XPS) and bulk (ICP, XFS) atomic ratios for Mn-Na-W/SiO₂ catalysts

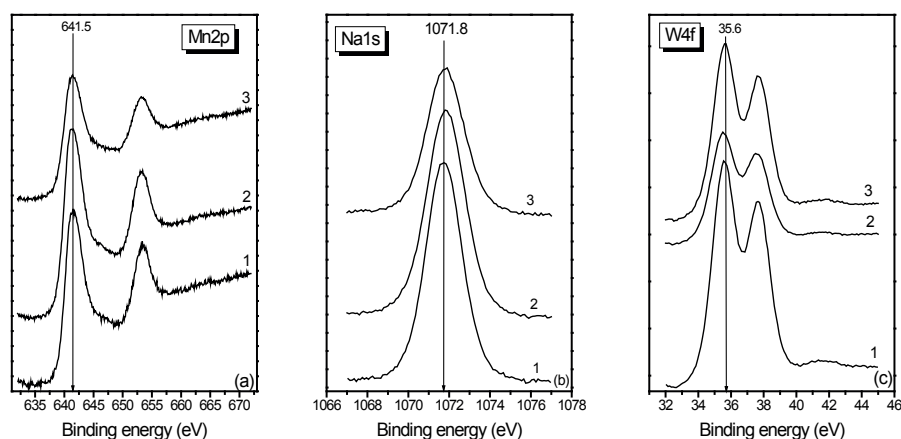| Sample	Mn/Si		Na/Si		W/Si	
	surface	bulk	surface	bulk	surface	bulk
Mn-Na-W/SiO₂ (I)	0.05	0.04	0.21	0.04	0.06	0.02
Mn-Na-W/SiO₂ (M)	0.05	0.04	0.20	0.05	0.03	0.02
Mn-Na-W/SiO₂ (P)	0.04	0.04	0.15	0.04	0.04	0.02

Fig. 1. XPS spectra in Mn2p (a), Na1s (b) and W4f (c) regions of the fresh catalysts: 1 – Mn Na-W/SiO₂ (I), 2 – Mn-Na-W/SiO₂ (M), 3 – Mn-Na-W/SiO₂ (P).
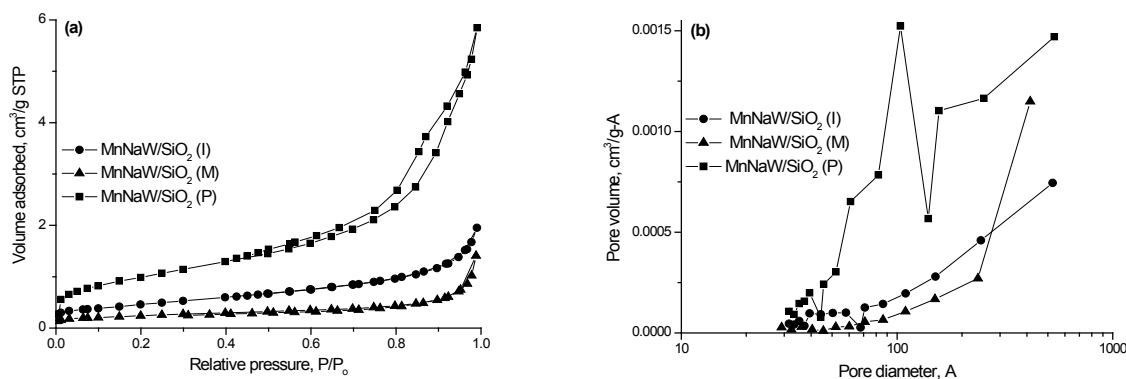
Fig. 2. N$_2$ adsorption-desorption isotherms (a) and the pore size distribution (b) for Mn-Na-W/SiO$_2$ catalysts.

The N$_2$ adsorption–desorption isotherms and the pore size distribution for Mn-Na-W/SiO$_2$ catalysts prepared by different methods are shown in Fig. 2. For Mn-Na-W/SiO$_2$ (I) and Mn-Na-W/SiO$_2$ (M) samples the type III isotherms without hysteresis loop indicate to the practically nonporous materials. In this case the surface area is mainly related to their external surfaces. For Mn-Na-W/SiO$_2$ (P) sample the type IV isotherm with a H1 hysteresis loop at relative pressure P/Po = 0.5–0.9 is observed which is associated with both textural and framework-confined mesopores [42, 43]. The wide pore size distribution is determined for all prepared samples (Fig. 2b).

The texture characteristics of Mn-Na-W/SiO$_2$ samples are listed in Table 1. In case of Mn-Na-W/SiO$_2$ (I) sample the addition of metal components to silica followed by calcination at 850 °C leads to a considerable decrease of specific surface area (from 320 to 1.6 m^2/g) and pore volume (from 1.1 to 0.003 cm^3/g) of support SiO$_2$. It can be explained by the transition of amorphous silica into crystalline phases during the calcination, which was previously reported [22, 25]. The observed texture characteristics (S$_{BET}$ ~ 1–3 m^2/g and V$_{pore}$ ~ 0.002–0.009 cm^3/g) of prepared Mn-Na-W/SiO$_2$ catalysts is in the good correlation with published data for Mn-Na-W/SiO$_2$ based materials [22, 25, 26]. As seen from data of the Table 1, the specific surface area and total pore volume increase in the following order: Mn-Na-W/SiO$_2$ (M) < Mn-Na-W/SiO$_2$ (I) < Mn-Na-W/SiO$_2$ (P). The specific surface area and total pore volume of Mn-Na-W/SiO$_2$ (P) sample is greater than those of Mn-Na-W/SiO$_2$ (I) and Mn-Na-W/SiO$_2$ (M) samples by more than 2 and 3 times, respectively. These results indicate that the textural characteristics of Mn-Na-W/SiO$_2$ are strongly affected by the preparation method and the calcination of the metal silsesquioxane mixtures produces more porous materials than those prepared by the impregnation or mixture slurry method.

Figure 3 shows the XRD patterns of α-cristobalite and Mn-Na-W/SiO$_2$ samples prepared by different methods and calcined at 850 °C for 6 h. The α-cristobalite (2θ = 25.6°, 33.2°, 36.7°, 42.2° and other, JCPDS 39-1425), tridymite (2θ = 24.1°, 27.1°, 35,2°, JCPDS 42-1401), Na$_2$WO$_4$ (2θ = 19.5°, 32.2°, 37.9°, 50.6 and 61.3°, JCPDS 12-0772) and Mn$_2$O$_3$ (2θ = 38.5°, 65.1°, JCPDS 41-1442) phases are observed in all studied catalyst after calcination at 850 °C (Fig. 3). However a strong decrease of intensity of diffraction pattern is observed for Mn-Na-W/SiO$_2$ (P) in comparison with those for Mn-Na-W/SiO$_2$ (I) and Mn-Na-W/SiO$_2$ (M) samples.

In case of reference samples, only Na-containing samples Mn-Na/SiO$_2$ and Na-W/SiO$_2$ show the phase transformation of silica into crystalline phases of α-cristobalite and tridymite after calcination at 850 °C. In the other samples Mn/SiO$_2$, W/SiO$_2$ and MnW/SiO$_2$ the SiO$_2$ support remains as amorphous silica after the analogous calcination. For Na-W/SiO$_2$ and Mn-W/SiO$_2$ samples the formation of crystalline Na$_2$WO$_4$ and MnWO$_4$ phases were observed, respectively. There are no any Mn- or W-containing crystalline phases in the Mn/SiO$_2$, W/SiO$_2$ and Mn-Na/SiO$_2$ samples.
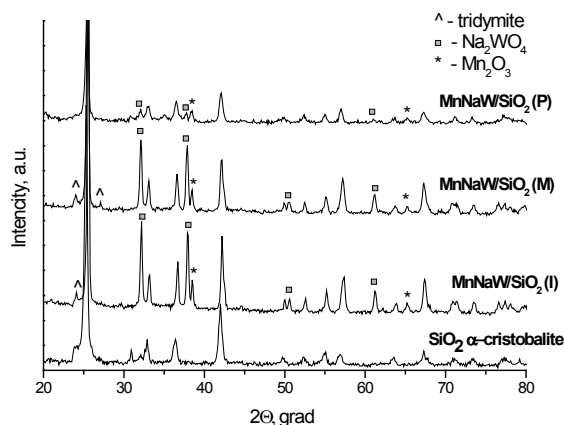

Fig. 3. Effect of preparation mode on phase composition of Mn-Na-W/SiO$_2$ catalysts. Calcination temperature is 850 °C.

Table 3
Observed XPS binding energies (eV) of catalyst components

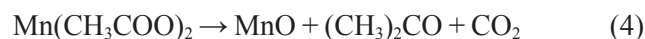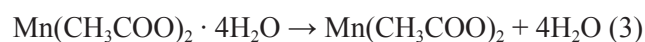| Sample	Mn2p	Na1s	W4f	Si2p	O1s (SiO$_2$)	O1s (MO$_x$)	C1s
Mn-Na-W/SiO$_2$ (I)	641.5	14071.75	35.55	103.3	532.7	530.5	284.8
Mn-Na-W/SiO$_2$ (M)	641.45	1071.8	35.5	103.3	532.7	530.7	284.7
Mn-Na-W/SiO$_2$ (P)	641.5	1071.8	35.6	103.3	532.7	530.6	284.8

Table 4
Phase composition of Mn-Na-W/SiO$_2$ catalysts: effect of calcination temperature

Sample	XRD data			
	T$_{calcination}$, °C			
	300 °C	500 °C	700 °C	850 °C
Mn-Na-W/SiO$_2$ (I)	amorphous SiO$_2$ MnWO$_4$	amorphous SiO$_2$ MnWO$_4$	α-cristobalite SiO$_2$ tridymite (traces) Na$_2$WO$_4$ Mn$_2$O$_3$	α-cristobalite SiO$_2$ tridymite (traces) Na$_2$WO$_4$ Mn$_2$O$_3$
Mn-Na-W/SiO$_2$ (M)	amorphous SiO$_2$ MnWO$_4$	amorphous SiO$_2$ MnWO$_4$	α-cristobalite SiO$_2$ tridymite (traces) Na$_2$WO$_4$ Mn$_2$O$_3$	α-cristobalite SiO$_2$ tridymite (traces) Na$_2$WO$_4$ Mn$_2$O$_3$
Mn-Na-W/SiO$_2$ (P)	amorphous SiO$_2$	amorphous SiO$_2$	α-cristobalite SiO$_2$	α-cristobalite SiO$_2$ tridymite (traces) Na$_2$WO$_4$ Mn$_2$O$_3$

The phase compositions of prepared Mn-Na-W/SiO$_2$ catalysts were also studied at variation of calcination temperature (Table 4). The diffraction pattern (broadened lines at d/n = 3.9 ≈ 4.1 and 2.9 ≈ 3.1 Å) of amorphous SiO$_2$ was determined for all samples calcined at 300–500 °C. In addition some peaks at d/n = 4.88, 2.98, 2.50 Å are observed only for catalyst prepared by impregnation and slurry mixed methods. These diffractions may be related to the presence of MnWO$_4$ phase. The transformation of amorphous SiO$_2$ to α-cristobalite and tridymite phases occurs after sample calcination at 700 °C. The formation of crystalline Na$_2$WO$_4$ and Mn$_2$O$_3$ phases is found after calcination at 700 and 850 °C for Mn-Na-W/SiO$_2$ (I)/Mn-Na-W/SiO$_2$ (M) and MnNaW/SiO$_2$ (P), respectively. It is noted that MnWO$_4$ phase is not detected by XRD in the Mn-Na-W/SiO$_2$ (I) and Mn-Na-W/SiO$_2$ (M) samples after calcination at 700–850 °C. Thus, the phase compositions of Mn-Na-W/SiO$_2$ samples prepared by impregnation or mixture slurry method are practically the same. In case Mn-Na-W/SiO$_2$ (P) sample prepared by the POSS nanotechnology the evolution of its phase composition has some peculiarities: i) absence of MnWO$_4$ phase after calcination at 300–500 °C; ii) formation of Na$_2$WO$_4$ and Mn$_2$O$_3$ crystalline phases at high-temperatures.

The particular features of formation of Mn-Na-W/SiO$_2$ catalyst prepared by different methods were studied by thermal analysis (Fig. 4). For the dried Mn-Na-W/SiO$_2$ (I) sample prepared by impregnation several temperature regions of weight loss can be noted (Fig. 4a): 50–200 °C (with endo-effects at T$_{DTA}$ ~ 100 and 170 °C with weight loss ~ 4.0% and ~ 1.3%, respectively); 200–500 °C (with exo-effect at T$_{DTA}$ ~ 285 °C and weight loss ~ 2.2% (at ~240 °C) and 3.0% (at ~275 °C)) and 500–1000 °C (with exo-effects at T$_{DTA}$ ~ 595 and 815 °C, and total weight loss ~ 3.7%).

According to literature data [46–48], decomposition of manganese acetate followed a two-step process. The first step was that of dehydration (Eq. 3), in which four molecules of water were eliminated in the temperature range 80–140 °C. In the second step of decomposition at 270–320 °C (Eq. 4), the anhydrous manganese acetate decomposed to manganese oxides and one molecule each of acetone and carbon dioxide were evolved as volatile products.
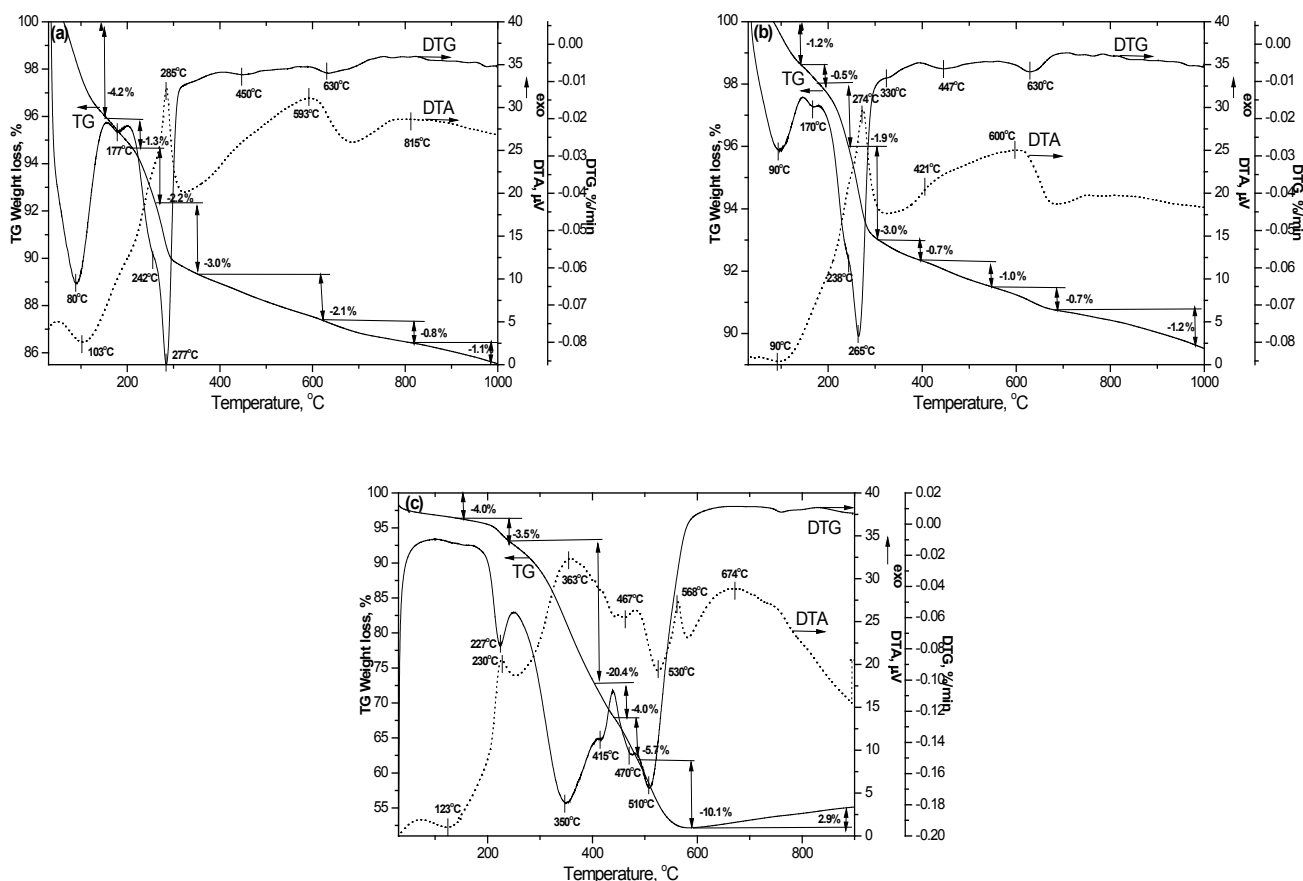
$$Mn(CH_3COO)_2 \cdot 4H_2O \rightarrow Mn(CH_3COO)_2 + 4H_2O \quad (3)$$

$$Mn(CH_3COO)_2 \rightarrow MnO + (CH_3)_2CO + CO_2 \quad (4)$$

Fig. 4. TG, DTG and DTA curves for Mn-Na-W/SiO$_2$ (I) (a), Mn-Na-W/SiO$_2$ (M) (b) and Mn-Na-W/SiO$_2$ (P) (c) catalysts dried at 120 °C.

TPD-MS study shows [46] that the destruction of acetates passes through two stages with maximum temperatures at c.a. 257 and 300 °C. The thermal degradation of manganese acetate in N$_2$ atmosphere leads to the formation of MnO, while that in air atmosphere leads to formation of Mn$_3$O$_4$ or Mn$_2$O$_3$ oxides. It is noted that thermal decomposition of MnO$_2$ to Mn$_2$O$_3$ (Eq. 5) proceeds at temperature region of 490–560 °C with endo-effect at 530 °C.

$$4MnO_2 \rightarrow 2Mn_2O_3 + O_2 \qquad (5)$$

Our TG-DTA measurement indicates that the DTA curve of the pure Mn(CH$_3$COO)$_2$ · 4H$_2$O in heating process shows three endothermic peaks at 73 °C, 92 °C and 124 °C corresponding to dehydration (with weight loss), two exothermal peaks at 307 °C and 334 °C corresponding to degradation of manganese acetate with formation of MnO$_x$ (with weight loss), weak thermal effects at 480 and 700 °C (with weight gain) related to MnO$_x$ oxygenation [49] and endo-effect at 970 °C with weight loss attributed to the decomposition of Mn$_2$O$_3$ to Mn$_3$O$_4$ [50].

The Na$_2$WO$_4$ · 2H$_2$O was characterized by following processes during thermal treatment: de-

hydration at ~ 100 °C with formation of Na$_2$WO$_4$ [51] and melting at 696 °C. Several polymorphs of sodium tungstate are known, only three existing at one atmosphere pressure [52]. They feature tetrahedral orthotungstate dianions but differ in the packing motif. Na$_2$WO$_4$ III is stable below 587.6 °C and crystallizes in the cubic spinel-type space group, Na$_2$WO$_4$ II exists stably only between 587.6 °C and 588.8 °C, when in turn transforms to Na$_2$WO$_4$ I which has orthorhombic lattice and melts at 695.5 °C. According to temperature-dependent Raman studies, it was established that crystal of Na$_2$WO$_4$ shows a phase transition occurring at ca. 560 °C [53]. These transitions are connected with tilting and/or rotations of the WO$_4$ tetrahedra, which leads to a disorder at the WO$_4$. Our TG-DTA measurement indicates that the DTA curve of the pure Na$_2$WO$_4$ in heating process shows three endothermic peaks at 120 °C, 596 °C and 700 °C corresponding to dehydration, solid–solid phase transition and solid–liquid phase transition (melting point, m.p.), respectively. Similar data was obtained for Na$_2$Mo$_{1-x}$W$_x$O$_4$ solid solution [54].

Silica crystallized at lower temperature in case of salt present (for example, Na$_2$WO$_4$ · 2H$_2$O) than

unmodified SiO_2 [16]. In addition, the dehydroxylation of different OH hydroxyl groups occurs during thermal treatment of silica [55, 56]. Our TG-DTA measurement indicates that the DTA curve of the pure Silica gel Davisil 646 in heating process shows two endothermic peaks at 100 °C corresponding to evaporation of physically adsorbed water from the silica sample (with weight loss 2.4 wt.%) and 344 °C related with dehydroxylation process of OH- groups from the silica surface. It is noted that according to TG data sample Silica gel Davisil 646 shows gradual weight loss in all temperature region 200–1000 °C. The weight loss in this temperature region is 4 wt.%.

Thus with a glance of TG-DTA data for unsupported individual compounds and literature data [46–56] it is proposed that during calcination of Mn-Na-W/SiO_2 (I) catalyst at 50–150 °C adsorbed and crystallized water was lost with formation of $Mn(CH_3COO)_2$ and Na_2WO_4. At temperature region of 200–400 °C $Mn(CH_3COO)_2$ decomposed to Mn oxide(s), which then transformed to Mn_2O_3 at ca. 450 °C. At 650 °C, probably, the melting of Na_2WO_4 occurred. At further temperature increase up to 850 °C, the α-cristobalite SiO_2 was formed. In addition at temperature above the 600 °C, dehydroxylation occurred, which caused the weight loss 2% in this region. The profiles of TG, DTG and DTA curves for dried Mn-Na-W/SiO_2 (M) sample prepared by mixture slurry method is on the whole similar to those for Mn-Na-W/SiO_2 (I) sample prepared by impregnation (Figs. 4a, 4b). So it can be concluded that genesis of dried Mn-Na-W/SiO_2 (I) and Mn-Na-W/SiO_2 (M) catalysts included decomposition of initial compounds and crystallization of new phases – Mn_2O_3 and α-cristobalite SiO_2.

Figure 4c shows TG, DTG and DTA curves for dried Mn-Na-W/SiO_2 (P) sample prepared by using metal containing silsesquioxanes as precursors. Non-isothermal temperature-programmed treatments of the fresh air-dried samples resulted in the appearance of exo- and endo-effects on the DTA curve (Fig. 4c). When the mixture of precursors was heated from room temperature up to 600 °C, sample lost 47.6% of its weight. The endo-effect observed at 120 °C was caused by the solvent removal. The exoeffects at $T_{DTA} \sim$ 230, 365 and 570 °C are probably related to the combustion of the organic groups from the precursor. According to mass spectra analysis during calcination of chromium containing polyhedral oligosilsesquioxane (c-C_5H_9)$_7$$Si_7O_9$(O-SiMe)$O_2CrO_2$ [33, 34] small amounts of CO, CO_2 and water were released starting at around 250 °C and slight consumption of oxygen was observed simultaneously; at 420 °C the amount of CO and CO_2 strongly increased while oxygen was consumed completely. The endo-effects at ~470 and ~530 °C are likely related to the decomposition of manganese-containing compound to MnO_2 followed by the transformation of MnO_2 to Mn_2O_3 [44, 45]. The exo-effect at $T_{DTA} =$ 675 °C is accompanied with the weight gain and may be associated with oxidation of metal-containing species of catalyst. According to XRD data (Fig. 3), the Mn-Na-W/SiO_2 (P) contains α-cristobalite SiO_2, Mn_2O_3 and Na_2WO_4 phases although it is difficult to determine their crystallization temperature region from our thermal analysis data. Thus, the genesis of the Mn-Na-W/SiO_2 (P) has the complex behavior pointing to the presence of the metal precursor decomposition with organic group burn-out and phase transformation.

The data of thermal analysis agree with the XRD data and indicate that the genesis of the Mn-Na-W/SiO_2 (P) prepared through the POSS nanotechnology considerably differs from genesis of samples prepared by incipient wet impregnation or slurry mixture method. The higher decomposition temperature of metal-POSS precursors in comparison with those of inorganic metal salts precursors (600 °C vs. 350 °C), as well as the presence of organic groups burn-out process influences the formation route of the crystalline phases in Mn-Na-W/SiO_2 catalyst. In addition, the presence of Si-O-M (M = Mn, Na or W) bonds in the metal-POSS precursors probably restricts the metal-metal interaction at low temperature of catalyst calcination and, consequently, crystalline phase formation.

Figure 5 shows TEM images of fresh Mn-Na-W/SiO_2 catalysts prepared by different methods. The Mn-Na-W/SiO_2 (I) catalyst prepared by impregnation consists of big globular SiO_2 particles of 5–10 μm in size. It is noted that small spherical SiO_2 particles of 10–20 nm in size are observed on the surface of large SiO_2 particles (Fig. 5a). There are MnO_x particles (up to 40 nm in size), W-containing particles (small WO_3 particles of 2–3 nm in size on the surface of amorphous Na_2WO_4 particles of 200 nm in size, Fig. 5b), $MnWO_4$ particles up to 40 nm and the oxide particles of high dispersion (Fig. 5c). As concerns the Mn-Na-W/SiO_2 (M) catalyst prepared by mixture slurry method, it consists of globular SiO_2 particles of 0.5–0.6 μm in size. In other respects this sample resembles the Mn-Na-W/SiO_2 (I) sample.

It is demonstrated that the fresh Mn-Na-W/SiO_2 (P) catalyst prepared through POSS nanotechnology consists of the globular aggregates (ca. 0.5–0.6 μm) and thin (ca. 30 nm) plates of SiO_2, on the surface of which particles of different composition and size are found (Figs. 5g-5i). In particular, there are

manganese oxide (Mn$_2$O$_3$, Mn$_3$O$_4$) spherical particles of 10–15 nm in size which are preferentially localized on the surface of thin SiO$_2$ plates (Figs. 5g, 5 h). There are also small MnWO$_4$ particles of 2–20 nm in size (Fig. 5i) and large amorphous Na$_2$WO$_4$ particles up to 200 nm in size. In addition, the oxide particles of high dispersion are observed. According to integral EDX data from different regions with oxide particles of high dispersion their composition are very variable.

It is demonstrated that the fresh Mn-Na-W/SiO$_2$ (P) catalyst prepared through POSS nanotechnology consists of the globular aggregates (ca. 0.5–0.6 µm) and thin (ca. 30 nm) plates of SiO$_2$, on the surface of which particles of different composition and size are found (Figs. 5g-5i). In particular, there are manganese oxide (Mn$_2$O$_3$, Mn$_3$O$_4$) spherical particles of 10–15 nm in size which are preferentially localized on the surface of thin SiO$_2$ plates (Figs. 5g, 5h). There are also small MnWO$_4$ particles of 2–20 nm in size (Fig. 5i) and large amorphous Na$_2$WO$_4$ particles up to 200 nm in size. In addition, the oxide particles of high dispersion are observed. According to integral EDX data from different regions with oxide particles of high dispersion their composition are very variable.

Thus the TEM study shows that preparation method affects mainly the morphology of SiO$_2$ support. In all samples both individual oxides (MnO$_x$, WO$_3$) and bimetal oxide phases (Na$_2$WO$_4$, MnWO$_4$) are found in addition to oxide particles of high dispersion. The MnO$_x$ and MnWO$_4$ particles are smaller in Mn-Na-W/SiO$_2$ (P) catalyst in comparison to those in Mn-Na-W/SiO$_2$ (I) and Mn-Na-W/SiO$_2$ (M) catalysts. It is noted that Na$_2$WO$_4$ phase is present as a rule in the form of amorphous compound on the surface of which the WO$_3$ small crystallites are observed. It is probable that Na$_2$WO$_4$ phase is not stable under irradiation during TEM study as it was previously shown for Gd$_2$(WO$_4$)$_3$ [57]. The crystalline phase of particles detected on the SiO$_2$ support by HRTEM does not exactly correspond to the phase composition detected by XRD. In particular, Mn$_3$O$_4$ and MnWO$_4$ phases are not observed by XRD (Fig. 3). Nevertheless according to TEM data this phase is present in all samples after calcination at 850 °C. A plausible reasons are that i) the particles had dimensions below the detection limit of XRD (ca. 3 nm); ii) low phase content; iii) complex XRD pattern of multicomponent materials in which some individual compounds have identical reflections.
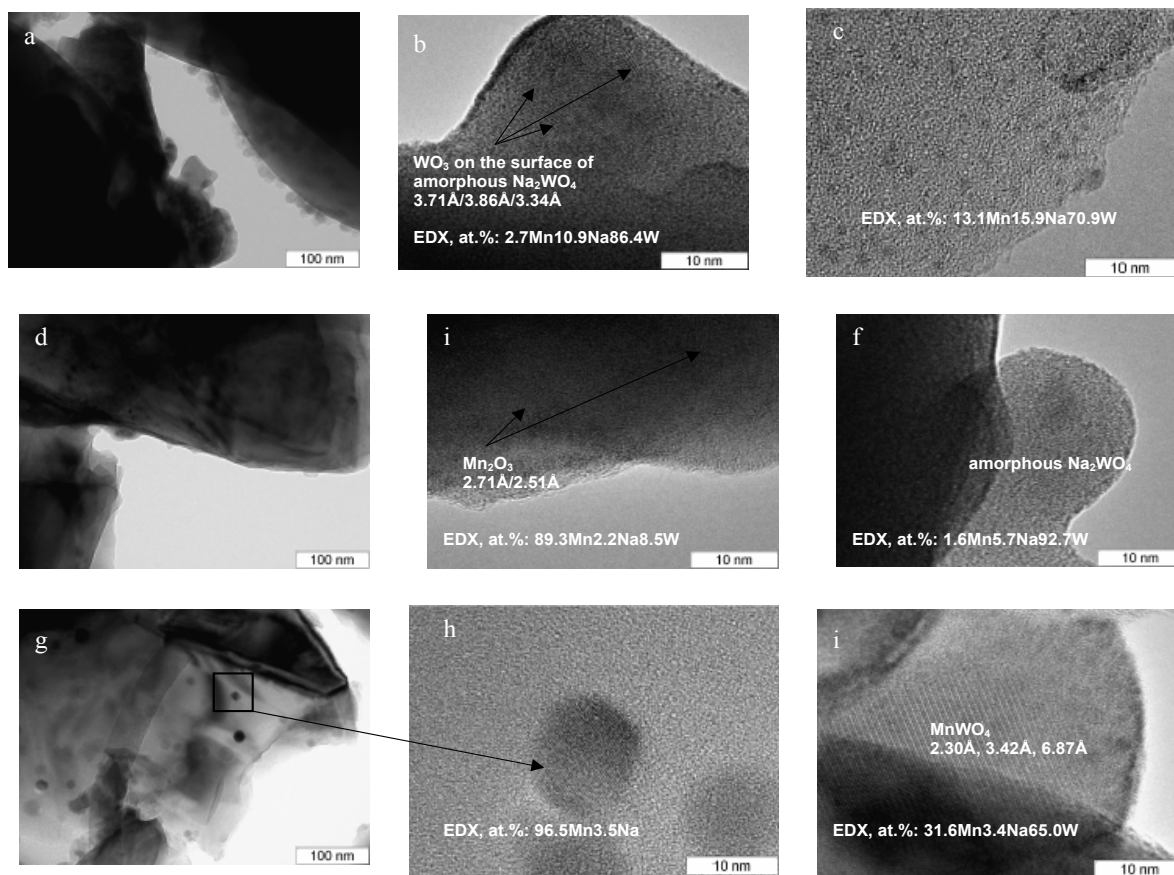

Fig. 5. TEM images of fresh Mn-Na-W/SiO$_2$ (I) (a-c), Mn-Na-W/SiO$_2$ (M) (d-f), Mn-Na-W/SiO$_2$ (P) (g-i) catalysts after calcination at 850 °C.
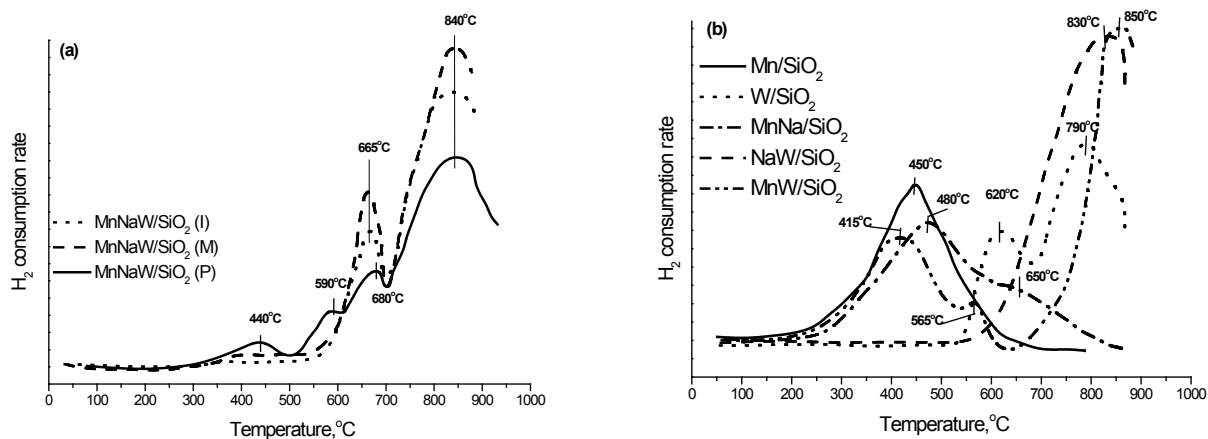
Fig. 6. H$_2$-TPR profiles of the fresh Mn-Na-W/SiO$_2$ catalysts (a) and reference samples (b).

Figure 6 shows the TPR profiles of the fresh Mn-Na-W/SiO$_2$ (I), Mn-Na-W/SiO$_2$ (M) and Mn-Na-W/SiO$_2$ (P) catalysts and reference samples Mn/SiO$_2$, W/SiO$_2$, Na-Mn/SiO$_2$, Na-W/SiO$_2$, Mn-W/SiO$_2$. The H$_2$-TPR profile of Mn/SiO$_2$ sample shows the broad peak at 450 °C (Fig. 6b). Bulk manganese oxides TPR peaks are observed to appear at temperatures in range of 130–500 °C [58]. It was suggested that manganese oxides are reduce of through the following steps:

$$MnO_2 \rightarrow Mn_3O_4 \rightarrow MnO$$

$$Mn_5O_8 \rightarrow Mn_2O_3 \rightarrow Mn_3O_4 \rightarrow MnO$$
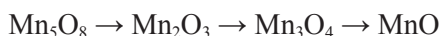
The temperature of the onset of reduction is the lowest for the highest oxide, increasing with decreasing oxidation state of the manganese [58]. For supported Mn oxides the reduction temperature varies in the wide range (TPR peaks at 290 and 400 °C [16, 59, 60], 350 [61], 650 °C [23], 575, 670 and 750 °C [62]) which can be related to different Mn oxidation states, dispersion or mode of Mn-support interaction. So, the broad peak of our Mn/SiO$_2$ sample is consistent with the previously reported data [16, 59, 60] and can be attributed to the stepwise reduction of supported Mn oxide species. However the H$_2$-TPR profile of Mn species reduction is changed by the presence of Na or W in the Mn/SiO$_2$ sample (Fig. 6b). In particular, upon W adding the main peak which was observed for Mn/SiO$_2$ sample at 450 °C shifts to the low-temperature region to 415 °C while at Na adding it shifts to the high-temperature region to 480 °C. In addition to the main peak shift, the shoulder appears at 650 and 565 °C for Mn-Na/SiO$_2$ and Mn-W/SiO$_2$ samples, respectively. As it was already mentioned above, in contrast to the Mn/SiO$_2$ sample which shows the amorphous silica phase, the Mn-Na/SiO$_2$

and Mn-W/SiO$_2$ samples contain crystalline α-cristobalite/trydimite and MnWO$_4$ phases, respectively.

The TPR profile of W/SiO$_2$ sample consists of two main peaks at 620 and 790 °C (Fig. 6b). The TPR profile obtained for WO$_3$ exhibits five peaks between 570 °C and 900 °C (572 °C, 635 °C, 707 °C, 871 °C and 900 °C), which were assigned to the reduction of WO$_3 \rightarrow$ W° in several steps via WO$_{3-x}$ sub-oxides (W$_{20}$O$_{58}$, W$_{18}$O$_{49}$, W$_{24}$O$_{68}$) and WO$_2$ [63, 64]. As a rule, the H$_2$–TPR patterns of W/SiO$_2$ catalysts present two peaks at 410–430 °C and 850–885 °C [65], 500 °C and 700 °C [16] or 530–590 °C and 630–640 °C [66]. The reduction at low-temperature region is not typical for W/SiO$_2$ sample. It is known that for supported W oxides the mode of H$_2$ consumption depends on WO$_3$ loading, structure and dispersion of the tungsten oxide species, conditions of calcination [65–67]. The decrease of temperature of W species reduction was assigned to (i) weakening of interaction between W species and support [60], (ii) increase in the dispersion of the tungsten oxide species [66], and (iii) the existence of the octahedrally coordinated species instead of tetrahedral tungstate species [67, 68]. So the two high-temperature peaks of our W/SiO$_2$ sample are consistent with the previously reported data [16, 66] and can be attributed to the stepwise reduction of supported WO$_3$ species. The addition of Na or Mn to W up shifts the W high-temperature reduction peak and leads to the disappearance of peak at 620 °C (Fig. 6b). The similar effect of up shifting of W reduction peak by Na addition was previously attributed to the strong interaction between Na and W components [16] and formation of other W species in the presence of Na ion [62]. It is also noted that Na presence induces the silica phase transition which is accompanied by S$_{BET}$ reduction and affects the metal species structure and dispersion.

The TPR profiles of Mn-Na-W/SiO$_2$ (I) and Mn-Na-W/SiO$_2$ (M) catalysts are practically similar to each other and exhibit low H$_2$ consumption at the temperature range 350–500 °C and two main peaks at 665 and 840 °C (Fig. 6a) that are close to the results described in literature [69, 70]. On the whole, the range of 450–550 °C correlates with Mn species reduction while the range of 650–850 °C correlates with reduction of W species. However as follows from Fig. 6b, the hindering of Mn species reduction is observed in the presence of Na or W metal in the sample. So the correlation of TPR peak at 665 °C with reduction of Mn or mixed Mn-W oxide species cannot be ruled out [19, 62, 71]. Thus the reduction peak at 665 °C represents the reduction of mixed Mn-W or W species while the peak at 840 ° C is attributed to the reduction of W species [16, 19, 58, 69, 71]. The TPR profiles of Mn-Na-W/SiO$_2$ (P) sample differs from those of Mn-Na-W/SiO$_2$ (I) and Mn-Na-W/SiO$_2$ (M) catalysts (Fig. 6a). It shows four peaks which may be assigned to the reduction of Mn oxides species (at 440 and 590 °C), mixed Mn-W oxide species (at 590 and 680 °C) and W oxide species (at 680 and 840 °C) [16, 19, 58, 69, 71]. It is noted that the H$_2$ consumption at T < 600 °C grows in the following order Mn-Na-W/SiO$_2$ (M) < Mn-Na-W/SiO$_2$ (I) < Mn-Na-W/SiO$_2$ (P) and reflects the existence of more easily reducible metal-oxide species in the Mn-Na-W/SiO$_2$ (P) sample.

Thus the TPR data indicate that the reduction pattern of tri-metallic Mn-Na-W/SiO$_2$ samples differs from the linear combinations of the TPR of reference samples. So there is change in redox properties of Mn and W oxide species in the tri-metallic system through the strong interaction between all the metal components in the Mn-Na-W/SiO$_2$ catalysts. The mode of H$_2$ consumption is affected by the preparation method of Mn-Na-W/SiO$_2$ catalyst. This can be evidence of the existence of different metal-containing species or metal-support interaction mode in the samples prepared by different methods. However, according to the XRD and TEM data all samples have similar phase composition but are at variance in the particle size. It is also noted that TEM results do not give quantitative data about amount of different metal-oxide species. Therefore the TPR data can point to different ratio between the individual oxides (MnO$_x$, WO$_3$), bimetal oxide phases (Na$_2$WO$_4$, MnWO$_4$) and oxide particles of high dispersion in the studied catalysts.

The electronic state of manganese was studied using Diffuse Reflectance Spectroscopy in ultra-violet, visible and near-infrared region (UV-Vis-NIR DRS). In the oxygen-containing catalysts,

manganese cations commonly have three oxidation degrees: 2+, 3+ and 4+. For Mn^{2+} cations (the electronic configuration d^5), the ground state term is the orbital singlet ^{6}S. In the octahedral crystal field, the ground state term of Mn^{2+} cations in a high-spin state is ^{6}A$_{1g}$. Let us consider two examples of complexes with Mn^{2+} cations in octahedral coordination (hereinafter Mn$^{2+}_{Oh}$). For the Mn(H$_2$O)$_6^{2+}$ complex, the following absorption bands are observed in the UV-Vis spectra: 18 700 (^{4}T$_{1g}$), 23 120 (^{4}T$_{2g}$), 24 960 (^{4}A$_{1g}$, ^{4}Eg(G)), 27 980 (^{4}T$_{2g}$(D)), 29 750 (^{4}Eg(D)), 32 960 (^{4}T$_{1g}$(P)) and 40 820 cm^{-1} (^{4}A$_{2g}$(F)) [72]. In this work, a precursor of manganese cations was represented by Mn(CH$_3$COO)$_2$ · 4H$_2$O salt, whose UV-Vis spectra (not displayed here) are characterized by the following absorption bands (in arbitrary units of the Kubelka-Munk function): 18 300 (^{4}T$_{1g}$), 22 600 (^{4}T$_{2g}$), 24 700 (^{4}A$_{1g}$, ^{4}Eg(G)), 27 600 (^{4}T$_{2g}$(D)), 29 400 (^{4}Eg(D)) and 32 500 cm^{-1} (^{4}T$_{1g}$(P)). As shown by the analysis of the UV-Vis spectra of Mn$^{2+}_{Oh}$ cations, the absorption bands caused by multiplicity-allowed d-d transitions are broad, while the absorption bands caused by multiplicity-forbidden d-d transitions are relatively narrow. According to the literature data [73], the absorption spectrum of Mn^{2+} cations in tetrahedral coordination (hereinafter Mn$^{2+}_{Td}$) is similar to the absorption spectrum of Mn$^{2+}_{Oh}$ cations shifted to the long-wavelength region. As was demonstrated in [72], the absorption spectra of tetrahedral Mn^{2+} complexes are characterized by three absorption regions: 19 000–25 000 cm^{-1} (transitions to components of ^{4}G term), 25 000–29 000 cm^{-1} (transitions to ^{4}P and ^{4}D terms), and 35 000–38 000 cm^{-1} (transitions to ^{4}F term).

For Mn^{3+} cations (the electronic configuration d^4), the ground state term is ^{5}D. In the octahedral crystal field, the ground state term of Mn^{3+} cations in a high-spin state is ^{5}Eg. Mn^{3+} cations in octahedral coordination are commonly characterized by a single absorption band at 21 000 cm^{-1}, and crystals – by the band in the region of 19 000–20 000 cm^{-1}, which is caused by the ^{5}E$_g$–^{5}T$_{2g}$ d-d transition of Mn$^{3+}_{Oh}$ cations [73]. However, in the majority of crystals, particularly in MgO, Mn^{3+} cations are in distorted octahedral coordination; in this case, both the static and the dynamic Jahn–Teller effects should be taken into account [73]. The energy levels related to splitting of higher terms of Mn^{3+} free cation (^{3}H, ^{3}P, ^{3}G and ^{3}D) weakly depend on the crystal field strength and can be observed in the spectrum as narrow and low-intense absorption bands in the region of 18 000–25 000 cm^{-1} [73]. Analysis of the literature data [72, 73] reveals that Mn$^{3+}_{Oh}$ cations typically have a broad absorption band in the region of 19 000 to 21 000 cm^{-1}.
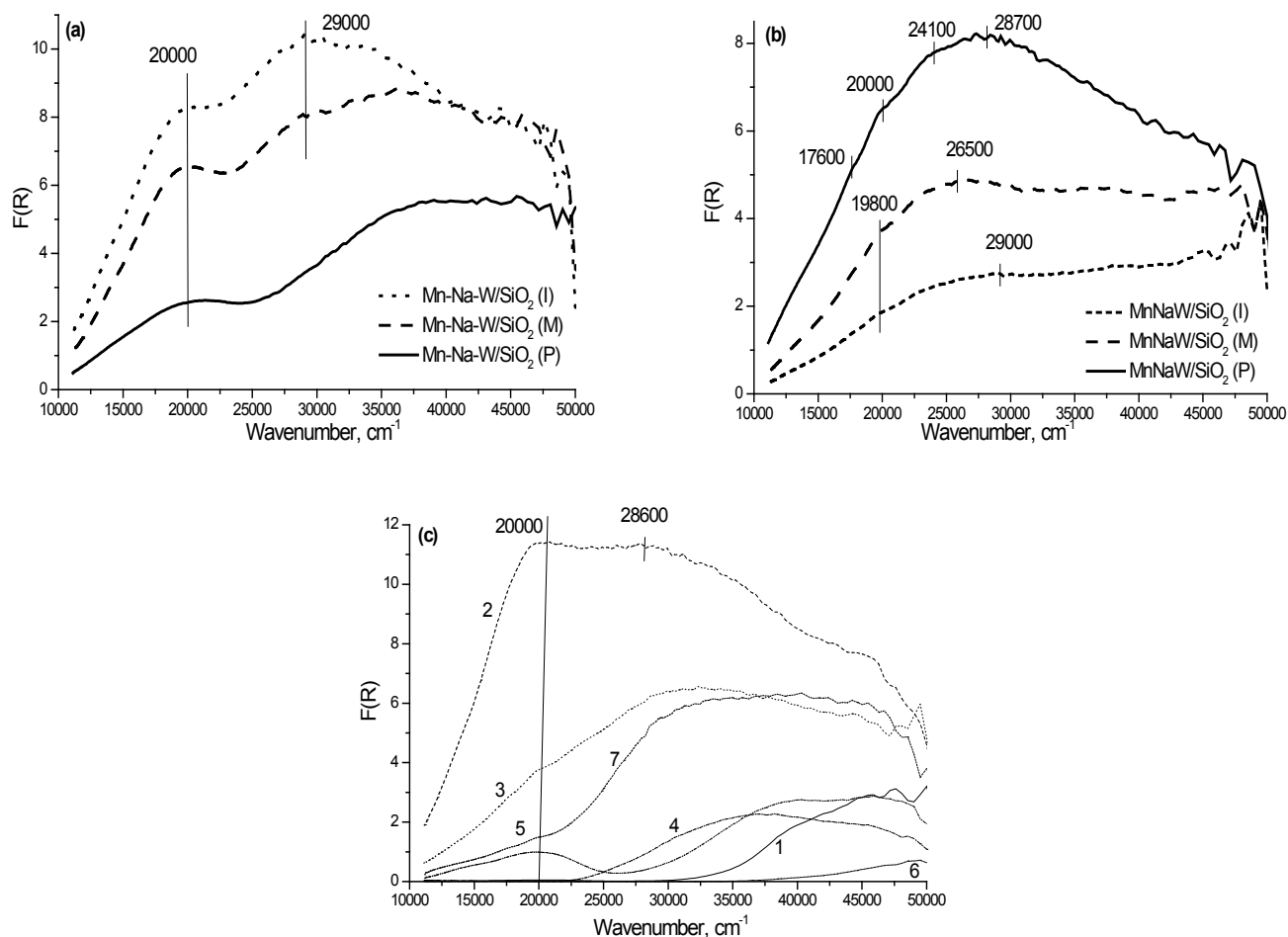
Fig. 7. UV-Vis diffuse reflectance spectra of Mn-Na-W/SiO$_2$ catalysts calcined at 300 °C (a), 850 °C (b) and α-cristobalite (1), Mn/SiO$_2$ calcined at 300 °C (2), Mn/SiO$_2$ (3),W/SiO$_2$ (4), Mn-Na/SiO$_2$ (5), Na-W/SiO$_2$ (6) and Mn-W/SiO$_2$ (7) reference samples (c) calcined at 850 °C.

For Mn^{4+} cations (the electronic configuration d^3), the ground state term is ^{4}F. In the octahedral crystal field, the ground state term of Mn^{4+} cations is ^{4}A$_{2g}$. According to [72], two broad and two narrow absorption bands will be observed in the absorption spectra of Mn^{4+} cations in octahedral coordination (hereinafter Mn$^{4+}_{Oh}$), since their absorption spectra are similar to those of Cr^{3+} cations in octahedral coordination, which are stabilized, for example, in the structure of α-Al$_2$O$_3$ corundum.

Thus, the analysis of the electronic state of manganese (its oxidation degree and coordination preferences) showed that Mn^{2+} cations in octahedral oxygen environment usually manifest themselves as a relatively large set of broad and narrow low-intense absorption bands, since they are caused by spin- and Laporte-forbidden d-d transitions [72], whereas in the case of tetrahedral coordination of Mn^{2+} cations, the absorption spectra will be similar to the spectra of the octahedral cations shifted to the long-wave region. Mn^{3+} cations usually have a broad absorption band in the visible spectral region

of 19 000 to 21 000 cm^{-1}. Mn^{4+} cations in octahedral oxygen coordination are characterized by two broad and two narrow absorption bands of different intensity in the visible spectral region.

Figure 7a displays the UV-Vis-NIR DRS spectra of Mn-Na-W/SiO$_2$ catalysts synthesized by different techniques and calcined at 300 °C. For all the samples, a broad absorption band with a maximum at 20 000 cm^{-1} is observed in the visible spectral region. It is known from the literature [72, 73] that the absorption band caused by d-d transition of Mn^{3+} cations in octahedral oxygen coordination is observed in the region of 20 000 cm^{-1}. Therewith, the absorption bands caused by charge transfer of the ligand-metal cations of d-elements are commonly seen in the region of 25 000–40 000 cm^{-1} [72]. A small red shift of the ligand-metal charge transfer band and an increase of absorption intensity in the region of 29 000 cm^{-1} in a series of samples P < M < I may indicate a coarsening of the Mn-containing particles comprising Mn^{3+} cations in octahedral coordination in this series of the synthesized samples.

An increase in the calcination temperature of Mn-Na-W/SiO₂ samples to 850 °C produced substantial changes in the UV-Vis-NIR DRS spectra (Fig. 7b), which reflect changes in the electronic state of manganese cations in the Mn-Na-W/SiO₂ catalysts. Weak absorption bands at 17 600 and 20 000 cm⁻¹ can be observed in the UV-Vis-NIR DRS spectrum of Mn-Na-W/SiO₂ (P) (Fig. 7b). These bands indicate a typical d-d transition of Mn^{3+}_{Oh} cations (20 000 cm⁻¹) and the d-d transition of electron to a higher ^3H term of the ground state of d⁴ ions in crystal structures [73]. It should be noted that in the absorption spectrum of Mn-Na-W/SiO₂ catalyst samples calcined at 850 °C there is no separation in the absorption caused by d-d transitions and ligand-metal charge transfer bands of Mn^{3+}_{Oh} cations. These samples are characterized by strong absorption over the entire spectral region with the absorption maximum at 25 000–30 000 cm⁻¹, which indicates most likely the formation of a crystal structure containing Mn^{3+}_{Oh} cations, for example, MnOOH.

Now let us consider in more detail the formation of crystal structures containing Mn^{3+} cations in octahedral coordination. Figure 7c displays the absorption spectra of the reference samples of different composition with modifying components deposited on the SiO₂ support. As seen from the absorption spectra of the initial cristobalite (Fig. 7c, curve 1), absorption of the entire system occurs in the region above 30 000 cm⁻¹; this allows a reliable interpretation of the absorption bands in the visible spectral region caused by the presence of the introduced elements. When a sample containing only the supported manganese (Fig. 7c, curve 2) was calcined at 300 °C, strong absorption was observed in the region above 15 000 cm⁻¹, which allowed us to isolate a maximum at 20 000 cm⁻¹ caused by stabilization of Mn^{3+}_{Oh} cations. Therewith, absorption in the region of 25 000–35 000 cm⁻¹ may indicate stabilization of the more coarse particles containing Mn^{3+}_{Oh} cations in comparison to the Mn-Na-W/SiO₂ catalyst samples (Fig. 7a). When the calcination temperature of Mn/SiO₂ was increased to 850 °C (Fig. 7c, curve 3), a more sharp drop in intensity of the absorption band at 20 000 cm⁻¹ was observed in the UV-Vis spectrum as compared to absorption in the region of 30 000 cm⁻¹ caused by the ligand-metal charge transfer of Mn^{3+}_{Oh} cations. Such drop in intensity may be related to a better ordering of Mn^{3+}_{Oh} cations upon temperature elevation in comparison with the low-temperature sample (Fig. 7c, curve 2). For the W/SiO₂ sample calcined at 850 °C (Fig. 7c, curve 4), total absorption of the entire system was observed in the region above 25 000 cm⁻¹, which was caused by appearance

of the ligand-metal charge transfer bands of W^{6+} cations. For the Mn-Na/SiO₂ sample calcined at 850 °C (Fig. 7c, curve 5), the absorption band at 20 000 cm⁻¹ and the absorption shoulder with a maximum at 15 000 cm⁻¹ are observed. Similar to the absorption spectra of Mn-Na-W/SiO₂ samples calcined at 850 °C (Fig. 7b), two absorption bands caused by d-d transitions of Mn^{3+}_{Oh} cations are observed in the visible region of the absorption spectrum of Mn-Na/SiO₂ sample calcined at 850 °C (Fig. 7c, curve 5). This suggests that this sample contains well ordered and uniformly distributed Mn^{3+}_{Oh} cations, most likely isolated from each other, which may be represented by dimers (but no more) that do not enter the composition of any crystal structure. A strong drop in the absorption intensity in the region above 30 000 cm⁻¹ is observed in the absorption spectrum of Na-W/SiO₂ sample (Fig. 7c, curve 6). The reason of this drop may be caused by low-temperature (850 vs. 1200 °C) transition of amorphous silica into crystalline phases (α-cristobalite and tridymite) during the calcination of SiO₂ modified by Na ions. It is noted that in case of samples without Na (W/SiO₂, Mn/SiO₂, Mn-W/SiO₂) the SiO₂ support retains the amorphous state.

In the visible region of the spectrum of Mn-W/SiO₂ sample calcined at 850 °C (Fig. 7c, curve 7), a sharp drop in intensity of the absorption bands at 15 000 and 20 000 cm⁻¹ caused by d-d transitions of Mn^{3+}_{Oh} cations is observed. Such a special absorption of Mn-W/SiO₂ sample calcined at 850 °C (Fig. 7c, curve 7) may indicate only that a major part of Mn^{3+}_{Oh} cations does not interact with W^{6+} cations. There is a good probability that Mn^{3+}_{Oh} and W^{6+} cations in this sample are isolated from each other, since the growth in intensity of the absorption bands caused by d-d transitions of cations of d-elements is strongly affected by both the anions in the first coordination sphere and the cations in the second coordination sphere. Most likely, a small part of Mn^{3+}_{Oh} cations facilitates the disordering of W^{6+} cations in the supported system, which leads to a dramatic, nearly threefold increase of absorption in the UV region of the spectrum.

Thus, when only manganese is deposited on the support, an increase in the calcination temperature to 850 °C leads to ordering of isolated Mn^{3+}_{Oh} cations with the formation of probable crystal structures. The introduction of Na^+ cations facilitates stabilization of Mn^{3+}_{Oh} cations in the isolated state at the same calcination temperature. The introduction of W^{6+} cations is favorable for retention of Mn^{3+}_{Oh} cations in the isolated state at the same calcination temperature; this is accompanied by strong disordering of W^{6+} cations in the supported system.
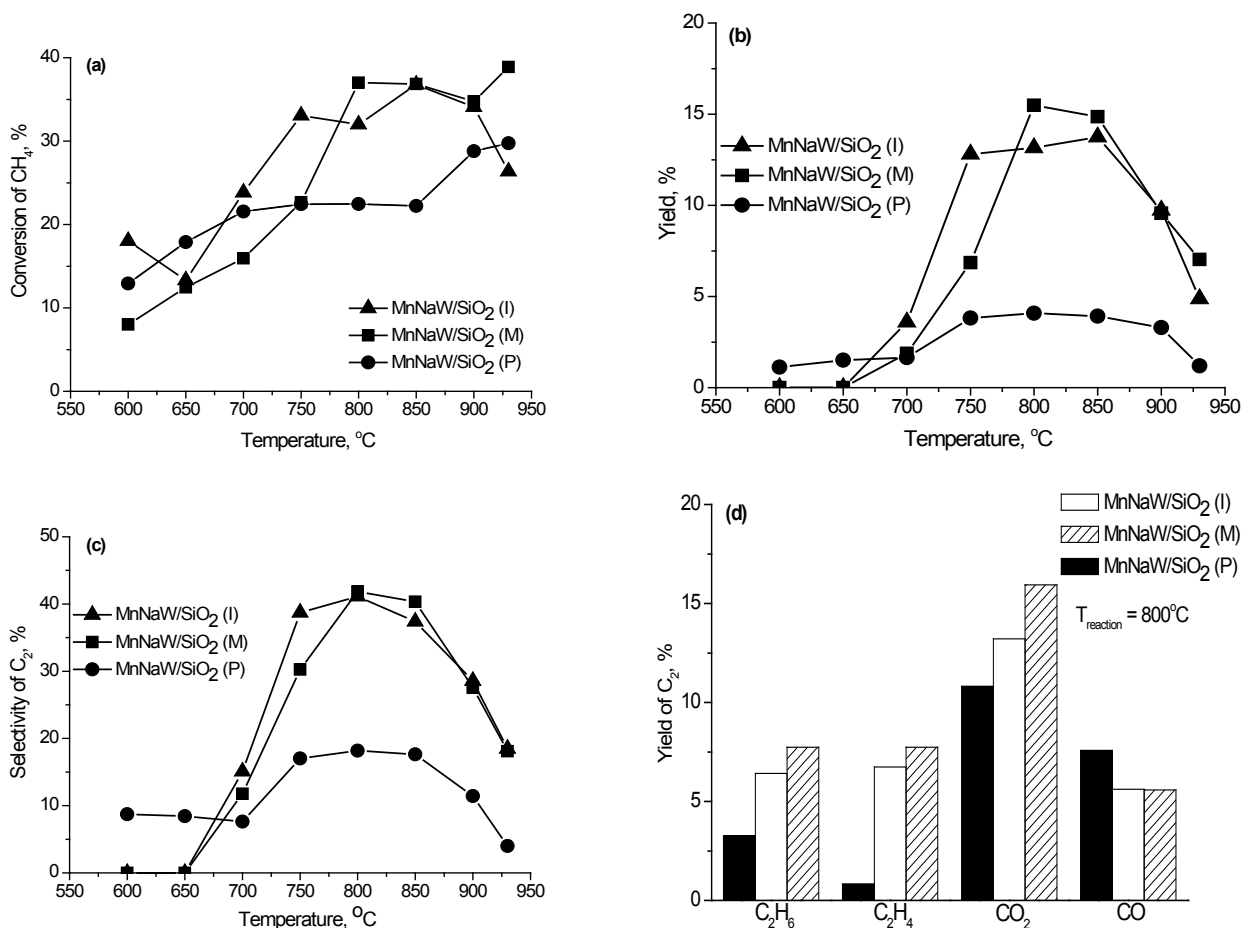
Fig. 8. Effect of preparation method on the catalytic activity of the Mn-Na-W/SiO$_2$ catalysts in the OCM reaction. Reaction conditions: CH$_4$: O$_2$: He = 4 : 1 : 2, 175 mLN/min.

3.2. OCM test

Figure 8 (a-d) shows catalytic performance of Mn-Na-W/SiO$_2$ samples at variation of preparation method. One can see that a temperature increase from 600 to 900 °C leads to an increase of methane conversion up to 30–35% (Fig. 8a). The change of oxygen conversion value with temperature growth has analogous character. The oxygen conversion is about 95% at temperature above 800 °C. The main reaction products are C$_2$H$_6$, C$_2$H$_4$, CO$_2$ and CO (Fig. 8d). The ethane yield increases with an increase of reaction temperature up to a maximum at 800–850 °C and then at T > 850 °C it decreases. The ethylene formation stats at reaction temperature above 800 °C and has a maximum at 900 °C. The C$_2$ yield and selectivity of C$_2$ hydrocarbons formation increases with an increase of the reaction temperature and has a maximum at ~800 °C (Figs. 8b, 8c). The CO and CO$_2$ yields increase with temperature growth in all studied temperature region.

One can see that the catalyst performance is strongly affected by the preparation method (Fig. 8). The samples prepared by incipient impregnation method and mixture slurry method provide practically similar catalytic performance while the sample prepared through POSS nanotechnology shows lower activity and selectivity. In particular, the C$_2$ yield at 800–850 °C is 4% and 15% for Mn-Na-W/SiO$_2$ (P) and Mn-Na-W/SiO$_2$ (M), respectively. The molar ratio C$_2$H$_4$/C$_2$H$_6$ is also considerably lower for Mn-Na-W/SiO$_2$ (P) (~0.2 at 800 °C) than that for Mn-Na-W/SiO$_2$ (M) sample (~1.0 at 800 °C). The obtained values of methane conversion (~40%) and C$_2$ yield (~15%) are comparable with those recently reported [10, 24].

All these results clearly confirm that the Mn-Na-W/SiO$_2$ catalyst performance in the OCM process can be regulated by the catalyst nanostructure design through the variation of the catalyst preparation mode. The Mn-Na-W/SiO$_2$ (I) and Mn-Na-W/SiO$_2$ (M) catalysts providing similar C$_2$ yield are characterized by similar phase composition, dispersion of particles of individual oxides (MnO$_x$, WO$_3$) and bimetal oxides (Na$_2$WO$_4$, MnWO$_4$) and reducibility, but they differ in SiO$_2$ morphology and textural properties. The Mn-Na-W/SiO$_2$ (P) catalyst providing the lowest C$_2$ yield among studied

samples marks out presence of unglobular SiO_2 particles, higher dispersion of MnO_x and $MnWO_4$ particles and more easily reducible metal oxide species. At present it is difficult to unambiguously establish exactly which of the listed properties has a crucial influence on the catalyst performance. As a rule, for the OCM reaction, as an example of homogeneous–heterogeneous reaction, the large surface areas and small particle sizes of the catalyst are not beneficial [64–76]. It is also noted that the reduction of manganese ions occurs during the OCM reaction [20, 76–79] along with the phase transformation from Mn_2O_3 to $MnWO_4$ [79]. However, there are controversial data concerning the role of Mn^{2+} species as well as that of $MnWO_4$ phase in the OCM reaction. It is demonstrated that the initial activity can be retained for periods up to 450 h along with the growth Mn^{2+}/Mn^{3+} ratio [20]. At the same time the Mn^{3+} is found as a proper oxidation state in the OCM reaction responsible for the methane activation [18, 26], and oxidized state of catalyst is necessary to maintain high C_2 selectivity [80]. So the existence of easily reducible metal oxide species seems to be not desirable for Mn-Na-W/SiO₂ catalyst. Further investigations of the effects of SiO_2 morphology, red-ox properties and $Mn_2O_3/MnWO_4$ ratio on the performance of Mn-Na-W/SiO₂ catalyst in the OCM reaction are required and these topics are the subject of our current study.

4. Conclusions

The series of Mn-Na-W/SiO₂ catalysts were prepared at variation of preparation mode (incipient wetness impregnation method, mixture slurry method, POSS nanotechnology) and their physical-chemical properties and catalytic performance in oxidative coupling of methane were comparatively studied. The data of XPS, BET, XRD, TG-DTA, HRTEM-EDX, TPR and UV-Vis Diffuse Reflectance indicate that the synthesis method has significant effect on the texture characteristics, SiO_2 morphology, dispersion and reducibility of metal oxide species in Mn-Na-W/SiO₂ catalysts. In all studied Mn-Na-W/SiO₂ samples both individual oxides (MnO_x, WO_3) and bimetal oxide phases (Na_2WO_4, $MnWO_4$) are found in addition to oxide particles of high dispersion. However the MnO_x and $MnWO_4$ particles are smaller in the catalyst prepared through the POSS nanotechnology (2–20 nm) in comparison to those in the catalysts prepared by impregnation or mixture slurry method (up to 40 nm). By DTA-TG and XRD analysis it is shown that particularities of catalyst precursors transformation during calcination determine the genesis of

Mn-Na-W/SiO₂ catalyst prepared by different methods. The UV-Vis Diffuse Reflectance indicates that Na^+ cations facilitate stabilization of octahedrally coordinated Mn^{3+}_{Oh} cations in the isolated state while Mn^{3+}_{Oh} promote the disordering of W^{6+} cations in the supported system. The TPR data reflects the existence of more easily reducible metal-oxide species in the catalyst prepared through the POSS nanotechnology. It was shown that methane conversion, products yield and selectivity of Mn-Na-W/SiO₂ in OCM were strongly affected by preparation method. The C_2 hydrocarbons yield at 800–850 °C increases from 4 to 15% when impregnation or mixture slurry method instead of POSS nanotechnology method of catalyst preparation is used.

Acknowledgments

References

[1]. I.Z. Ismagilov, E.V. Matus, V.V. Kuznetsov, M.A. Kerzhentsev, N. Mota, R.M. Navarro, J.L.G. Fierro, A.J.J. Koekkoek, G. Gerritsen, H.C.L. Abbenhuis, Y.A. Zaharov, Z.R. Ismagilov, International Scientific Journal for Alternative Energy and Ecology 13-14 (2016) 13–30.

[2]. E.V. Matus, I.Z. Ismagilov, O.B. Sukhova, V.I. Zaikovskii, L.T. Tsikoza, Z.R. Ismagilov, J.A. Moulijn, Ind. Eng. Chem. Res. 46 (2007) 4063–4074.

[3]. I.Z. Ismagilov, E.V. Matus, V.V. Kuznetsov, N. Mota, R.M. Navarro, M.A. Kerzhentsev, Z.R. Ismagilov, J.L.G. Fierro, Catal. Today 10 (2013) 10–18.

[4]. I.Z. Ismagilov, E.V. Matus, V.V. Kuznetsov, N. Mota, R.M. Navarro, S.A. Yashnik, I.P. Prosvirin, M.A. Kerzhentsev, Z.R. Ismagilov, J.L.G. Fierro, Appl. Catal. A 481 (2014) 104–115.

[5]. I.Z. Ismagilov, E.V. Matus, V.V. Kuznetsov, M.A. Kerzhentsev, S.A. Yashnik, I.P. Prosvirin, N. Mota, R.M. Navarro, J.L.G. Fierro, Z.R. Ismagilov, Int. J. Hydrogen Energy 39 (2014) 20969–21006.

[6]. E.V. Matus, O.B. Sukhova, I.Z. Ismagilov, L.T. Tsikoza, Z.R. Ismagilov, Reac. Kinet. Catal. Let. 98 (2009) 59–67.

[7]. N.T. Vasenin, V.F. Anufrienko, I.Z. Ismagilov, T.V. Larina, E.A. Paukshtis, E.V. Matus, L.T.

Tsikoza, M.A. Kerzhentsev, Z.R. Ismagilov, Top. Catal. 32 (2005) 61–70.

[8]. J.H. Lunsford, Catal. Today 63 (2000) 165–174.

[9]. I.Z. Ismagilov, E.V. Matus, S.D. Vasil'ev, V.V. Kuznetsov, M.A. Kerzhentsev, Z.R. Ismagilov, Kinetics and Catalysis 56 (2015) 456–465.

[10]. S. Arndt, T. Otremba, U. Simon, M. Yildiz, H. Schubert, R. Schomäcker, Appl. Catal. A 425–426 (2012) 53–61.

[11]. O.V. Buyevskaya, M. Rothaemel, H.W. Zanthoff, M. Baerns, J. Catal. 146 (1994) 346–357.

[12]. S. Pak, P. Qiu, J.H. Lunsford, J. Catal. 179 (1998) 222–230.

[13]. U. Zavyalova, M. Holena, R. Schlögl, M. Baerns, ChemCatChem. 3 (2011) 1935–1947.

[14]. L. Olivier, S. Haag, H. Pennemann, C. Hofmann, C. Mirodatos, A.C. Veen, Catal. Today 137 (2008) 80–89.

[15]. Z.C. Jiang, C.J. Yu , X.P. Fang, S.B. Li, H.L.Wang, J. Phys. Chem. (1993) 12870–12875.

[16]. H.S. Chen, J.Z. Niu, B. Zhang, S.B. Li, Acta Phys. Chim. Sinica 17 (2001) 111–115.

[17]. D. Wang, M.P. Rosynek, J.H. Lunsford, J. Catal. 155 (1995) 390–402.

[18]. Hou, Y. Cao, W. Xiong, H. Liu, Y. Kou, Ind. Eng. Chem. Res. 45 (2006) 7077–7083.

[19]. Z.C. Jiang, H. Gong, S.B. Li, Stud. Surf. Sci. Catal. 112 (1997) 481–490.

[20]. Y. Kou, B. Zhang, J. Niu, S. Li, H.Wang, T.Tanaka, S. Yoshida, J. Catal. 173 (1998) 399–408.

[21]. S. Ji, T. Xiao, S. Li, C. Xu, R. Hou, K.S. Coleman, M.L.H Green, Appl. Catal. A 225 (2002) 271–284.

[22]. A. Palermo, J.P.H. Vazques, A.F. Lee, M.S. Tikhov, R.M. Lambert, J. Catal. 177 (1998) 259–266.

[23]. J.G. Wu, S.B. Li, J. Phys. Chem. 99 (1995) 4566–4568.

[24]. A.G. Dedov, G.D. Nipan, A.S. Loktev, A.A. Tyunyaev, V.A. Ketsko, K.V. Parkhomenko, I.I. Moiseev, Appl. Catal. A: Gen. 406 (2011) 1–12.

[25]. J. Wang, L. Chou, B. Zhang, H. Song, J. Zhao, J. Yang, S. Li, J. Mol. Catal. A: Gen. 245 (2006) 272–277.

[26]. W. Zheng, D. Cheng, F. Chen, X. Zhan, J. Natur. Gas Chem. 19 (2010) 515–521.

[27]. R. Ghose, H.T. Hwang, A. Varma, Appl. Catal. A: Gen. 452 (2013) 147–154.

[28]. I.Z. Ismagilov, E.V. Matus, V.V. Kuznetsov, M.A. Kerzhentsev, I.P. Prosvirin, R.M. Navarro, J.L.G. Fierro, G. Gerritsen, E. Abbenhuis, Z.R. Ismagilov, Eurasian Chemico-Technological Journal 17 (2015) 105–118.

[29]. K. Wada, T. Mitsudo, Catal. Surv. Asia 9 (2005) 229–241.

[30]. A.J. Ward, A.F. Masters, T. Maschmeyer, Chapter 3 Metallasilsesquioxanes: Molecular Analogues of Heterogeneous Catalysts, 2011. P. 135–166 In: C. Hartmann-Thompson (ed.), Applications of Polyhedral Oligomeric Silsesquioxanes, Advances in Silicon Science 3, DOI 10.1007/978-90-481-3787-9_3, Springer Science+Business Media B.V.

[31]. N. Maxim, A. Overweg, P.J. Kooyman, A. Nagy, R.A. Santena, H.C.L. Abbenhuis, J. Mater. Chem. 12 (2002) 3792–3798.

[32]. N. Maxim, Metal silesquioxanes as precursors to microporous metallosilicates PhD, Technische Universiteit Eindhoven, 2002.

[33]. N. Maxim, H.C.L. Abbenhuis, P.J. Stobbelaar, B.L. Mojet, R.A. van Santen, Phys. Chem. Chem. Phys. 1 (1999) 4473–4477.

[34]. N. Maxim, P.C.M M. Magusin, P.J. Kooyman, J.H.M.C. van Wolput, R.A. van Santen, H.C.L. Abbenhuis, Chem. Mater. 13 (2001) 2958-2964.

[35]. R. Murugavel, P. Davis, V. Shete, Inorg. Chem. 42 (2003) 4696–4706.

[36]. J.H. Scofield, Electron Spectrosc. Relat. Phenom. 8 (1976) 129–137.

[37]. B.R. Strohmeier, D.M. Hercules, J. Phys. Chem. 88 (1984) 4922–4929.

[38]. V. Bayer, R. Podloucky, C. Franchini, Phys. Rev. B 76 (2007) 165428.

[39]. C.D. Wagner, Faraday Discuss. Chem. Soc. 60 (1975) 291–300.

[40]. S.C. Moulzolf, S. Ding, R.J. Lad, Sens. Actuat. B 77 (2001) 375–382.

[41]. S.F. Ho, S. Contarini, J.W. Rabalais, J. Phys. Chem. 91 (1987) 4779–4788.

[42]. T.-D. Nguyen-Phan, M.B. Song, E.J. Kim, E.W. Shin, Micropor. Mesopor. Mater. 119 (2009) 290–298.

[43]. T.R. Pauly, Y. Liu, T.J. Pinnavaia, S.J.L. Billinge, T.P. Rieker, J. Am. Chem. Soc. 121 (1999) 8835–8842.

[44]. N.A.M Deraz, G.A El-Shobaky, Thermochim. Acta 375 (2001) 137–145.

[45]. W.M. Shaheen, M.M. Selim, J. Therm. Anal. Calorim. 59 (2000) 961–970.

[46]. V.G. Makhankova, O.V. Khavryuchenko, V.V. Lisnyak, V.N. Kokozay, V.V. Dyakonenko, O.V. Shishkin, B.W. Skelton, J. Jezierska, J. Solid State Chem. 183 (2010) 2695–2702.

[47]. M.A. Mohamed, S.A. Halawy, Thermochim. Acta, 242 (1994) 173–186.

[48]. M. Afzal, P.K. Butt, H. Ahmad, J. Therm. Anal. 37 (1991) 1015–1023.

[49]. M.I. Zaki, M.A. Hasan, L. Pasupulety, K. Kumari, Thermochim. Acta 303 (1997) 171–181.

[50]. Y. Suzuki, K. Muraishi, H. Ito, Thermochim. Acta 258 (1995) 231–241.

[51]. G.G.T. Guarini, L. Dei, Thermochim. Acta 250 (1995) 85–96.

[52]. C.W.F.T. Pistorius, Chem. Phys. 44 (1966) 4532–4537.

[53]. C.L. Lima, G.D. Saraiva, P.T.C. Freire, M. Maczka, W. Paraguassu, F. F. de Sousa, J.M. Filho, J. Raman Spectrosc. 42 (2011) 799–802.

[54]. X.-L. Sun, W.-X. Li, X.-M. Wang, X.-P. Jing, Phase Trans. 83 (2010) 491–500.

[55]. J.M. Kim, S.M. Chang, S.M. Kong, K.-S. Kim, J. Kim, W.-S. Kim, Ceram. Intern. 35 (2009) 1015–1019.

[56]. P. Staszczuk, Colloids Surfaces A: Phys. Eng. Asp. 105 (1995) 291–303.

[57]. Y. Zeng, Z. Li, L. Wang, Y. Xiong, CrystEngComm 14 (2012) 7043–7048.

[58]. F. Kapteijn, L. Singoredjo, A. Andreini, J.A. Moulijn, Appl. Catal. B: Environ. 3 (1994) 173–189.

[59]. H. Yin, Y. Ding, H. Luo, H. Zhu, D. He, J. Xiong, L. Lin, Appl.Catal. A 243 (2003) 155–164.

[60]. H. Treviño, G.-D. Lei, W.M.H. Sachtler, J. Catal. 154 (1995) 245–252.

[61]. Y. Wang, Z. Song, D. Ma, H.Y. Luo, D.B. Liang, X.H. Bao, J. Mol. Catal. A: Chem. 149 (1999) 51–61.

[62]. A. Malekzadeh, A. Khodadadi, A. K. Dalai, M. Abedini, J. Natur. Gas Chem. 16 (2007) 121–129.

[63]. C. Bigey, L. Hilaire, G. Maire, J. Catal. 184 (1999) 406–420.

[64]. C. Bigey, L. Hilaire, G. Maire, J. Catal. 198 (2001) 208–222.

[65]. Q. Zhao, S.-L. Chen, J. Gao, C. Xu, Trans. Met. Chem. 34 (2009) 621–627.

[66]. A. de Lucas, J.L. Valverde, P. Canizares, L. Rodriguez, Appl. Catal. A 172 (1998) 165–176.

[67]. V. Logie, G. Maire, D. Michel, J.-L. Vignes, J. Catal. 188 (1999) 90–101.

[68]. V.M. Benitez, C.A. Querini, N.S. Figoli, Appl. Catal. A 252 (2003) 427–436.

[69]. S.M.K. Shahri, A.N. Pour, J. Natur. Gas Chem. 19 (2010) 47–53.

[70]. S. Mahmoodi, M.R. Ehsani, M. Hamidzadeh, Iran. J. Chem. Chem. Eng. 30 (2011) 29–36.

[71]. Z. Gholipour, A. Malekzadeh, R. Hatami, Y. Mortazavi, A. Khodadadi, J. Natur. Gas Chem. 19 (2010) 35–42.

[72]. A.B.P. Lever, Inorganic Electronic Spectroscopy.-2nd ed.; Elsevier: Amsterdam – Oxford – New York – Tokyo, 1987.

[73]. D.T. Sviridov, R.K. Sviridova, Yu.F. Smirnov. Optical Spectra of Transition Metal Ions in Crystals. Nauka, Moscow, 1976, 266 p.

[74]. M. Gharibi, F.T. Zangeneh, F.Yaripour, S. Sahebdelfar, Appl.Catal. A 443–444 (2012) 8–26.

[75]. V.S. Arutunov, O.V. Krylov, Oxidative conversion of methane.-Moscow: Nauka, 1998.-361 p.

[76]. K. Langfeld, B. Frank, V.E. Strempel, C. Berger-Karin, G. Weinberg, E.V. Kondratenko, R. Schomäcker, Appl. Catal. A 417-418 (2012) 145–152.

[77]. M. Ioffe, P. Bosch, T. Viveros, H. Sanchez, Y.G. Borodko, Mater. Chem. Phys. 51 (1997) 269–275.

[78]. Y.T. Chua, A.R. Mohamed, S. Bhatia, Appl. Catal. A. 343 (2008) 142–148.

[79]. U. Simona, O. Gorke, A. Berthold, S. Arndt, R. Schomacker, H. Schubert, Chem. Eng. J. 168 (2011) 1352–1359.

[80]. T.P. Tiemersma, M.J. Tuinier, F. Gallucci, J.A.M. Kuipers, M. van Sint Annaland, Appl. Catal. A 433–434 (2012) 96–108.